Transmission Electron Imaging and Diffraction of Asbestos Fibers in a Scanning Electron Microscope

Jason D. Holm* and Elisabeth Mansfield

National Institute of Standards and Technology, Applied Chemicals and Materials Division, Boulder, CO, 80305

*Corresponding author: jason.holm@nist.gov

Abstract

Test protocols for airborne clearance of asbestos abatement sites define the collection, imaging and quantification of asbestos with transmission electron microscopy (TEM). Since those protocols were developed 35 years ago, scanning electron microscope (SEM) capabilities have significantly improved and expanded, with improvements in image spatial resolution, elemental analysis, and transmission electron diffraction capabilities. This contribution demonstrates transmission electron imaging and diffraction using NIST Asbestos Standard Reference Materials and a conventional SEM to provide comparable identification and quantification capabilities in the SEM as the current regulatory methods based on TEM techniques. In particular, we demonstrate that the 0.53 nm layer line spacing that is characteristic of asbestos can be quantified using different detection methods, and that other identifying diffraction signatures of chrysotile are readily obtained. The results demonstrate a viable alternative to the current TEM-based methods for asbestos identification and classification.

Keywords: Asbestos, electron diffraction, SEM, 4D STEM, STEM-in-SEM

Synopsis: Transmission electron imaging and diffraction analysis of asbestos is straightforward in SEMs, thereby improving analytical accessibility and enabling field-deployable test methods with potential for reduced instrumentation cost compared to TEM.

Introduction

Asbestos is a class of naturally occurring, fibrous, hydrated silicates. At least six types of asbestos have been used in modern applications, including chrysotile, crocidolite, amosite, tremolite, actinolite and anthophyllite. Chrysotile, a serpentine form of asbestos, exists as short (< 2.5 cm), fine (approx. 250 Å diameter) crystalline fibers. It is the most common of the different asbestos types found in commercial applications.[1,2] The remaining five belong to the amphibole material class, with amosite and crocidolite having been used more frequently than the others. Prior to the Industrial Revolution, asbestos properties including fire and chemical (acid) resistance were utilized. The number and diversity of applications grew as manufacturing capabilities improved, leading to widespread use of asbestos in building materials, railroad and automotive applications, and personal protection equipment for firefighting, among others. Although it was known as early as the 1920s that airborne asbestos exposure caused serious health problems, applications continued to grow until the early 1970s when the Clean Air Act of 1970 and the Asbestos National Emission Standards for Hazardous Air Pollutants (NESHAP) of 1973 were established.[3,4] Shortly thereafter, asbestos use began to fade as the health concerns and regulations forced manufacturers to find alternative material options. More recently, water pipes made of asbestos reinforced cement are nearing the end of their anticipated lifespans, and the release of fibers into domestic water supplies is of concern to several.[5] Although there is no consensus on health issues associated with asbestos ingestion, fibers released into domestic water supplies can become airborne through commonplace activities such as household humidification or lawn watering.

In the U.S., the Environmental Protection Agency (EPA) is responsible for establishing regulations and test methods for airborne asbestos monitoring. The most recent EPA specification, Guidelines for Conducting the AHERA TEM Clearance Test to Determine Completion of an Asbestos Abatement Project, was published 35 years ago.[6] Other methods for identifying and classifying asbestos fibers for environmental health and safety concerns have also been established and have evolved over several decades.[7] All of them specify the use of transmission electron microscopy (TEM) for analysis.[8-11] In the early years of test protocol development, it was decided that the TEM was the logical choice for asbestos fiber analysis because of the better spatial resolution than the scanning electron microscope (SEM), the capacity to observe the tubular structure of chrysotile fibers, and perhaps most importantly, the ability to obtain electron diffraction patterns (DPs) using selected area electron diffraction (SAED) that would allow fibers to be classified according to their crystal structure.[12,13] Today, SAED is central to all TEM-based test protocols because it allows asbestos fibers to be differentiated from non-asbestos fibers, and different asbestos types to be discerned from one another (i.e., serpentine or amphibole).

Although SEMs could be equipped for transmission imaging when the protocols were developed, the practice was uncommon and not typically used for fiber analysis.[14] Since then, image spatial resolution, elemental analysis, and transmission electron diffraction capabilities (all of which are utilized in the most comprehensive asbestos fiber analyses) have vastly improved in SEMs. For example, modern field-emission SEMs have spatial resolution close to or better than

1 nm using secondary electron (SE) detectors. This is sufficient to observe extremely fine asbestos fibers, including the tubular structure of chrysotile which can exhibit fiber diameters as small as a few tens of nm. Moreover, the surface and 'bulk' morphology of individual fibers and fiber bundles can also be imaged using SEs to differentiate asbestos fibers from non-asbestos fibers, as well as to differentiate between asbestos types in some instances. For example, amphibole asbestos fibers often have frayed or split ends, while glass fibers often have fractured or bulbous ends.[15] Differentiating tubular chrysotile fibers from other asbestos types is also straightforward for an experienced operator using only an SE detector. Although TEMs can be equipped with SE detectors that enable the examination of fiber surface topography, they are extremely rare on modern microscopes. Energy dispersive X-ray (EDX) spectrometers have been a mainstay of SEM platforms for decades. Modern detectors are more efficient than those available when the original test protocols were developed, and the time required to obtain a spectrum with sufficient signal-to-noise ratio (S/N) is generally less than a few minutes. Automated techniques have also been developed to identify asbestos using EDX-SEM.[16]

A recent trend in SEMs is the use of transmission electron imaging and diffraction techniques.[17] For example, semiconductor-style detectors like one of the detectors used in this contribution can provide transmission electron images with strong contrast and single nanometer spatial resolution making the tubular structure of chrysotile fibers observable and some defects in amphibole asbestos visible as well. Pixel array detectors (i.e., digital diffraction cameras) are also seeing increasing use in SEMs.[18] These pixelated detectors can be used in different ways. For example, DPs can be obtained from precise locations on the sample by positioning the electron beam at specific locations. Alternatively, the beam can be rastered over a region of interest (ROI) to obtain a DP in a manner akin to SAED. Emerging microscopy techniques such as 4-dimensional scanning transmission electron microscopy (4D STEM) can also be employed in an SEM to enable automated data collection and analyses over large areas including entire TEM grids.[19] The idea behind 4D STEM is that at each beam raster position a full DP is collected, and the complete set of DPs can be used for various offline imaging- and diffraction-based analyses.[20] The data collection procedure is practically identical to that used in electron backscatter diffraction (EBSD) except that 4D STEM applications are not limited to those that utilize only Kikuchi scattering. Although conventional and transmission EBSD studies have been done on asbestos,[21,22] 4D STEM methods have not to our knowledge. 4D STEM is well suited to examine asbestos for several reasons. For example, consider chrysotile, the most common type of asbestos used in commercial applications. Chrysotile fibers do not require tilting to specific zone axes to obtain DPs that can be used for the most rigorous TEM classification purposes. Therefore, samples can be scanned in an automated manner without the need for an operator to tilt different fibers. Chrysotile fibers are also notably susceptible to electron beam damage.[23] 4D STEM is especially appealing in this regard because the beam is scanned over a region of interest once and beam dwell times ranging from only a few milliseconds to a few tens of milliseconds are required to obtain meaningful DPs that can be analyzed offline in numerous ways and multiple times.

In this contribution, we demonstrate different methods to image and obtain from asbestos in a conventional field emission SEM using electrons transmitted through the sample. We show how the SEM can be used to obtain DPs from individual and large numbers of fibers in a straightforward manner. The information in this manuscript demonstrates how these imaging

and diffraction methods can provide information equivalent to that specified in TEM-based asbestos regulatory test protocol.

Materials and Methods**

Asbestos samples examined here comprise NIST SRM 1866, Common Commercial Asbestos (i.e., chrysotile, amosite, and crocidolite). Figure 1 shows the samples in their 'as-received' form. Slurries of each asbestos type were prepared by placing a small amount of fiber sample in isopropanol and grinding using a mortar and pestle. In general, less than 2 ml isopropanol was required to obtain fibers sufficiently dispersed for analysis. A drop of each slurry was pipetted onto ultrathin carbon sample support grids (Ted Pella, Prod. #01844 or #01824) and allowed to dry in air. Prior to sample pipetting, some sample support grids were sputtered with a thin layer of gold and then heated at 80 °C for 20 minutes to provide an internal polycrystalline diffraction reference.

Figure 1. Images of neat NIST SRM 1866 asbestos samples.

A Zeiss Gemini 300 Variable Pressure SEM was used for electron imaging and diffraction. Fiber morphology and topography images were recorded with the off-axis SE detector using primary electron beam energies ranging from 2 keV to 30 keV, and the Zeiss aSTEM detector (i.e., an annular semiconductor-style detector) was used to record transmission images at beam energies from 15 keV to 30 keV. Transmission electron diffraction patterns and 4D STEM datasets were recorded using a digital camera (Thorlabs CS135MU) and the apparatus shown schematically in Figure 2.[19] As shown in the figure, electrons transmitted through and diffracted by the sample strike a scintillator causing it to emit photons in a pattern that replicates the DP. A mirror and lens assembly directs that pattern outside the SEM vacuum chamber to the digital camera which records an image of the DP.

Three approaches were used to collect DPs: snapshot, video, and 4D STEM. In snapshot mode, the beam was rastered over a specific ROI or positioned at specific location on the sample (i.e., on a single fiber) and a single DP was recorded. In video mode, the camera was set to continuously record images while the electron beam was manually positioned at different points on the sample. Here, an image of the sample was first obtained with the SEM, and then the SEM imaging mode was changed to spot mode in which the user can place the beam at any location in the field of view as the video is recorded. Camera vendor software was used without modification for these two modes. In 4D STEM mode, LabVIEW was used to synchronize the camera with the SEM scan coils, and to automatically record DPs at each beam raster position in a user-defined ROI. A thorough description of the apparatus and technique can be found

elsewhere.[19] 4D STEM datasets were analyzed offline using MATLAB to extract various images and DPs.

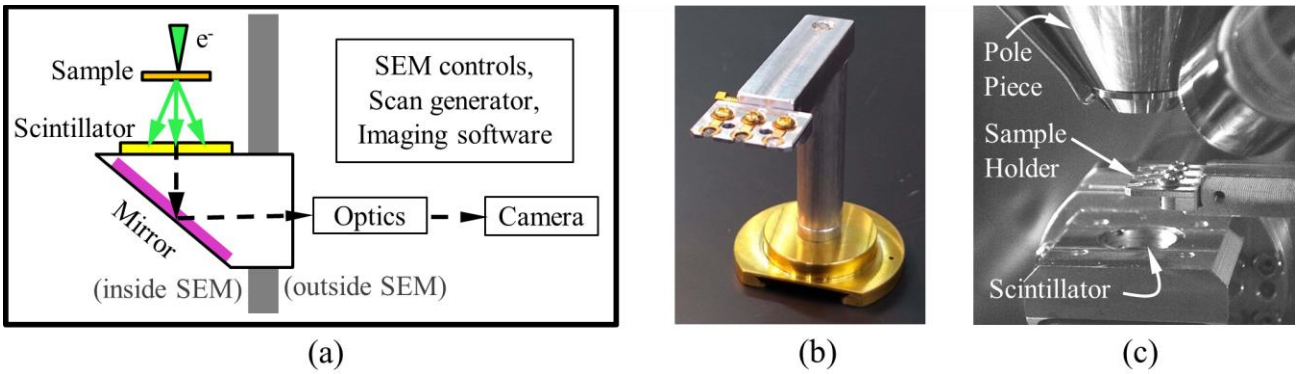

Figure 2. Experimental apparatus. (a) Schematic of the transmission diffraction detector setup. b) The 3-slot sample holder. (c) An interior view of the SEM vacuum chamber showing the locations of the different components.

A 3-slot sample holder attached to the SEM stage (Fig. 2b) was used to position samples between the SEM pole piece and the scintillator (Fig. 2c). A polycrystalline aluminum (pAl) sample (Ted Pella, Prod. #619) was kept in one of the three sample slots and used as an external diffraction reference. When pAl was used as a diffraction reference, it was essential that the imaging conditions and working distance were the same as those used for the asbestos sample. To that end, DPs were first obtained from different spots on a well-focused image of the asbestos sample. Without changing the focus settings, the aluminum reference sample was then brought to the optic axis, and moved vertically until the pAl microstructure was in focus. The beam was then rapidly rastered across a small area in the center of the field of view (FoV) to obtain a ring DP of the polycrystalline aluminum sample that could be used as a reference.

Results

Chrysotile

Chrysotile is the most common form of asbestos in commercial products.[1,2] It is also the most straightforward of the three asbestos varieties considered here to analyze by electron diffraction because the DP does not change with fiber orientation, and therefore tilting to specific zone axes is not required. Regardless of how chrysotile fibers are rotated about the long fiber dimension, the DP will exhibit closely spaced spots arranged in periodic rows called layer lines. The periodicity between the layer lines corresponds to the 0.53 nm spacing between layers in the tubular, or more accurately, the scroll-like chrysotile fiber structure.[24] In addition to the layer lines, chrysotile DPs also exhibit characteristic streaking on layer lines other than the central line that passes through the direct beam. These two characteristics, layer line spacing and streaking, are strong indications of the presence of chrysotile fibers.[25,26] Chrysotile results shown here are used to demonstrate conventional and non-conventional transmission imaging and diffraction techniques in an SEM.

Secondary electron images of chrysotile fiber bundles and small fiber fragments are shown in Fig. 3a and Fig. 3b. The large spaghetti-like bundles in Fig. 3a are typical of the chrysotile SRM after brief grinding by hand. Fig. 3b shows chrysotile fibers dispersed on an ultrathin carbon substrate with a thin layer of sputtered gold. Even at 2 keV beam energy, small fibers can be observed on the bright Au background. Fig. 3c and Fig. 3d show higher magnification images where the tubular chrysotile structure can be seen. Notice the slight difference in the appearance of the fiber surfaces between the two images. In Fig. 3c, the beam was rastered over the FoV once and the fibers exhibited a relatively smooth surface. In Fig. 3d, the beam was rastered over the FoV several times and the fibers exhibited a blistered surface that is characteristic of electron beam damage.[24] This observation is important because even at beam energies typical of an SEM (i.e., $\leq$ 30 keV) the DP can rapidly fade and disappear with increasing electron dose, rendering diffraction results unusable, and making multiple diffraction studies of the same fiber(s) impractical.

As explained elsewhere,[24,27,28] the observed beam damage is not a simple effect of temperature rise due to electron irradiation. Rather, multiple damage mechanisms are likely to occur simultaneously and at different rates. To those ends, different mitigation strategies including reducing the sample temperature and changing the beam accelerating voltage have been studied. For example, a recent study showed that by lowering the sample temperature the damage rate was reduced in anthophyllite fibers as quantified by measuring how the Mg/Si ratio changed using EDX.[27] Although that study did not specifically examine diffraction pattern spot intensity decay rates, they did briefly note that cooling the specimen had no effect on the rate at which the DP faded. Altering the electron beam energy is another strategy often invoked as a method to reduce beam damage. Reducing the beam energy may be a viable strategy for minimizing knock-on damage, but the predominant damage mechanisms here are more likely radiolytic and charge-related damage.[28] Reducing the voltage is likely to increase the damage rate for these mechanisms.[29] The most straightforward strategy to reduce beam damage is to decrease the beam dose. This is where 4D STEM is beneficial because it only requires one scan of a FoV to acquire a dataset that can be repeatedly analyzed offline.

Figure 3e and Figure 3f show a pair of 30 keV images recorded simultaneously with the SE detector and the aSTEM transmission detector, respectively. The inset in Fig. 3f shows the detector segments used to generate the unconventional contrast in the transmission image. Here, the white segments were set to positive polarity, black segments were set to negative polarity, and gray segments were not used. The opposing polarity detection mode produces the unusual contrast in the transmission image: some fibers exhibit dark walls while others exhibit bright walls depending on the sample orientation with respect to the detector segments. Regardless of the uncommon contrast mechanism, the strong contrast produced by the tube walls suggests nearly every fiber in the FoV exhibits the tubular structure. Many fibers also exhibit varying contrast between the outermost edges that could be due to adventitious debris within the tubes, defects in the tubular structure, or more likely, electrons scattered from tube walls oriented in other directions (vide infra).

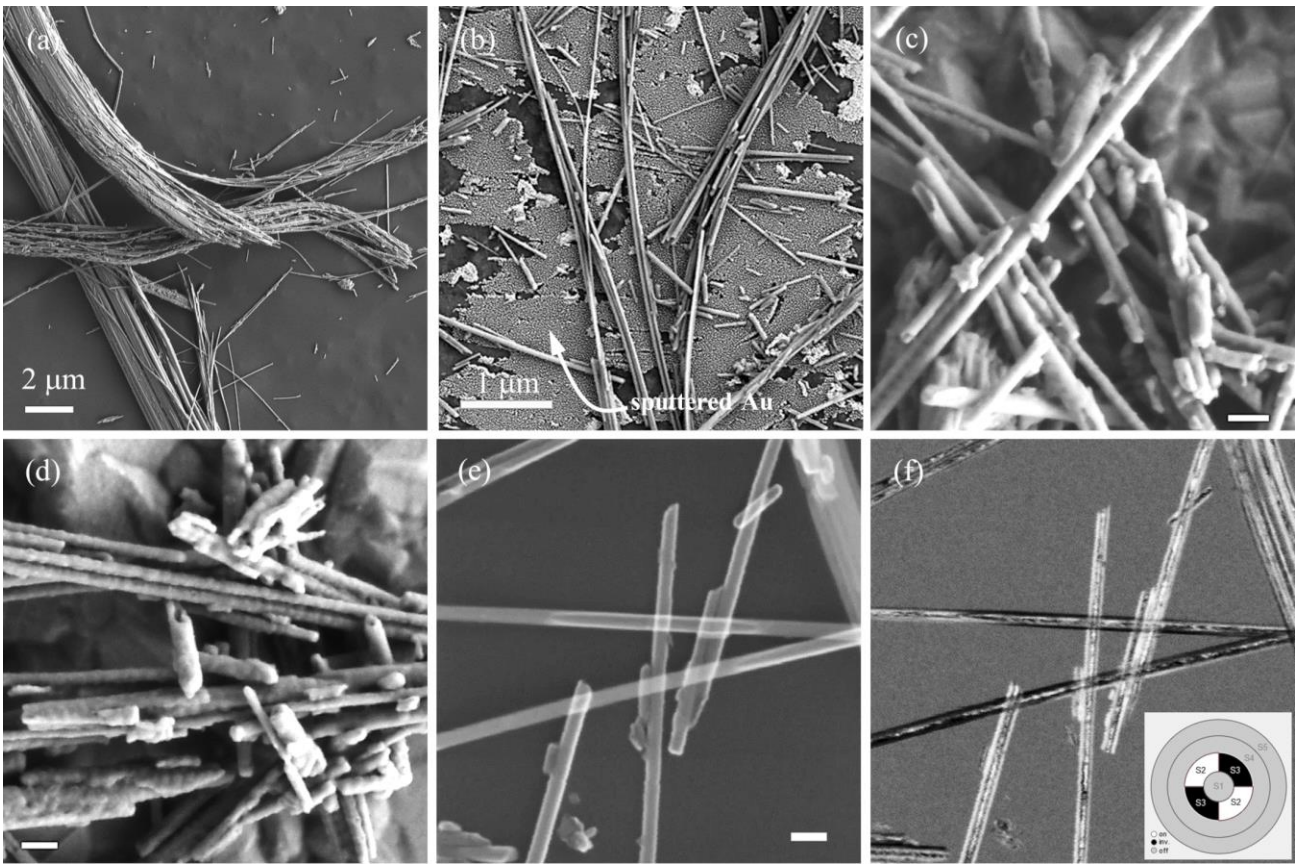

Figure 3. Chrysotile images. SE images (2 keV) of fiber bundles and fragments on (a) an ultrathin carbon substrate, and (b) an Au-sputtered substrate. The inset arrow points to the sputtered Au. (c) Fibers showing the tube-like structure. The substrate is the copper support structure of the TEM grid. (d) Fibers with blistered surfaces after several electron beam scans. (e) A 30 keV SE image of fiber fragments on an ultrathin carbon substrate, and (f) a non-conventional dark-field transmission image recorded simultaneously with the aSTEM transmission imaging detector. The inset diagram shows how the detector segments were configured to generate the image contrast. Unlabeled scale bar lengths = 100 nm.

Figure 4 shows chrysotile DPs combined with the sputtered Au and the pAl diffraction references. In both images the characteristic electron diffraction features of chrysotile can be observed (i.e., layer lines with the correct spacing and streaking on lines other than the one coincident with the direct beam). Both DPs were extracted from videos that were recorded as the primary electron beam was manually positioned at different points on the sample. Figure 4a shows a DP obtained from a single fiber on an Au-sputtered carbon substrate. The inset red cross indicates the center of the direct beam (i.e., the (000) spot), the dashed red arc indicates the faint Au (111) diffraction ring, and the solid red line indicates the distance between the chrysotile ($\bar{1}10$) and (110) reflections (i.e., twice the separation between layer lines).

The characteristic 0.53 nm layer spacing (i.e., the distance between (100) planes, $d_{\text{chrysotile(100)}}$) can be obtained from basic diffraction geometry[30]:

$$d_{\text{chrysotile(100)}} = (d_{\text{Au(111)}} \times L_{\text{Au(111)}}) / L_{\text{chrysotile(100)}}.$$

Here, $d_{\text{Au(111)}}$ = 0.235 nm (i.e., the distance between Au (111) planes based on the lattice constant a_o = 0.409 nm). The other two parameters are obtained directly from DP measurements: $L_{\text{Au(111)}}$ is the distance from the center of the direct beam to the Au (111) ring (98.2 px), and $L_{\text{chrysotile(100)}}$ is the distance between layer lines (86.8 px / 2 = 43.4 px). The $d_{\text{chrysotile(100)}}$ spacing calculated from these measurements is 0.532 nm. The chrysotile (002) reflection can be used for more comprehensive characterization,[31] and to discriminate other fibers such as halloysite, vermiculite scrolls, and palygorskite that can be mistaken for chrysotile.[11] Here, the distance between (000) and (002) is 31.5 px, giving $d_{\text{chrysotile(002)}}$ = 0.734 nm. For comparison, the spacings for chrysotile (100) and (002) planes calculated based on the monoclinic structure and lattice parameters obtained from X-ray diffraction are approximately 0.533 nm and 0.733 nm, respectively.

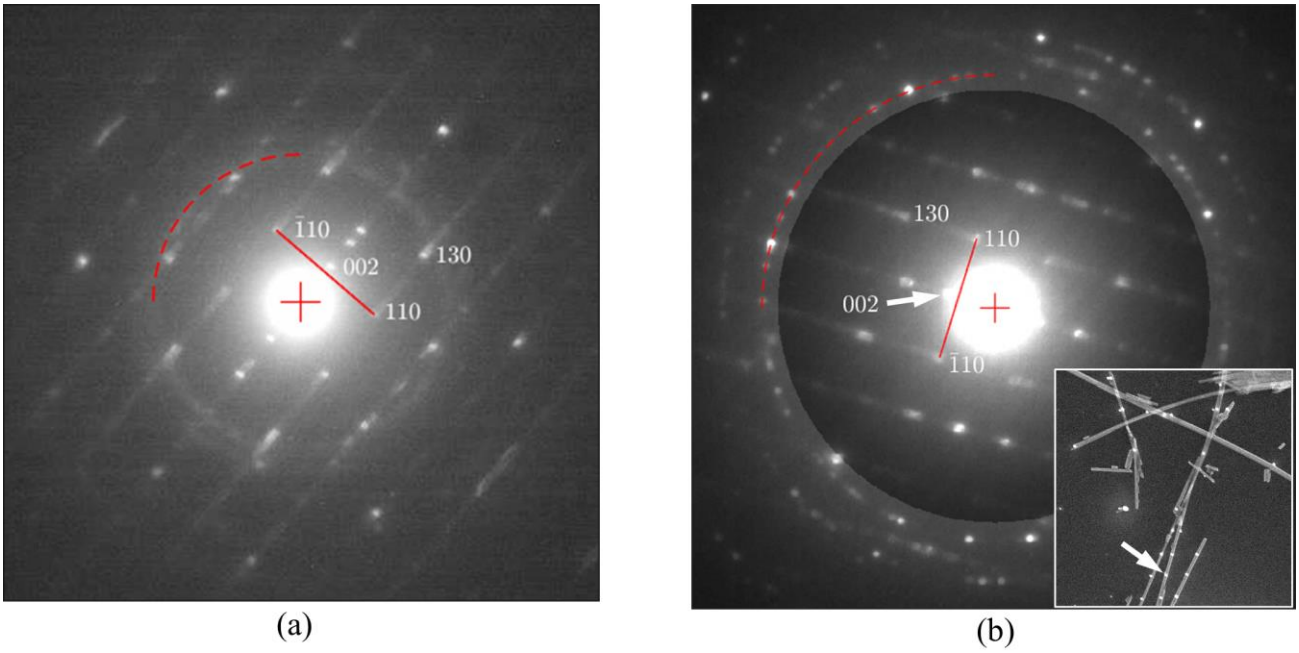

Figure 4. DPs from single chrysotile fibers recorded at 30 keV with the sample on (a) an Au-sputtered ultrathin carbon substrate, and (b) on an ultrathin carbon substrate with a superimposed polycrystalline Al reference DP recorded under identical conditions. The arrow in the inset SE image (horizontal FoV = 3.7 μm) shows the location/fiber from which the DP was obtained. The distinct white spots at different locations in the inset SE image are due to carbon buildup where the beam was positioned on the sample.

As an alternative to using an Au-sputtered support grid as an internal diffraction reference, Figure 4b shows a composite image comprising two DPs: one obtained by positioning the electron beam at a single spot on one chrysotile fiber (indicated by the arrow in the inset SE image), and another obtained from the pAl reference sample recorded under experimentally similar conditions. Before the DPs were digitally combined, a circular area slightly smaller than

the Al (220) diffraction ring was cropped from the aluminum DP to avoid saturating features of interest in the chrysotile DP. Note that the insets/markers indicate similar parameters to those indicated in Fig 4a, except the red arc is now superimposed on the Al (220) reflection. The $d_{\text{chrysotile(100)}}$ spacing obtained from this image is 0.533 nm based on the calculated Al (220) reference lattice spacing (0.143 nm), the distance from the center of the direct beam to the $L_{\text{Al(220)}}$ ring (231.4 px), and the distance between layer lines (124.4 px /2 = 62.2 px). Although the direct beam appears to largely overlap the (002) spot, making measurements of the spot position challenging, $d_{\text{chrysotile(002)}}$ can also be obtained using the (004) spot which is approximately 90.5 px from the center of the direct beam. The $d_{\text{chrysotile(002)}}$ spacing obtained from this measurement is 0.732 nm.

The results of Figure 4 demonstrate that an SEM can be used to record DPs that enable measurements of interplanar spacings from individual chrysotile fibers. Moreover, both internal (i.e., Au-sputtered grids) and external (i.e., pAl) diffraction references can be used to obtain nearly identical measurement results. If sharper diffraction rings with stronger contrast are desired when using sputtered Au as a reference, the primary electron beam can be positioned immediately adjacent to the fiber in question to obtain a ring DP exclusively from the Au. This way, the DPs are still recorded at effectively identical conditions, and a longer beam dwell time can be used to obtain an Au reference DP that exhibits distinct diffraction rings without damaging the beam-sensitive chrysotile fibers.

Figure 5 shows 4D STEM results obtained from chrysotile on an ultrathin carbon substrate. Here, the SEM magnification was 20,000× and a 30 keV beam (20 μm beam-limiting aperture) was rastered across the RoI in a 400 × 400 array of equally spaced positions. Camera exposure time was 15 ms at each raster position and the active camera area was set to 400 px × 400 px, and binned (3×3) to obtain 133 px × 133 px DPs. As a baseline, Figure 5a shows a low pixel density SE image (615 px × 615 px) of the RoI. For comparison, Figure 5b shows a marginal bright-field (BF) transmission image of the same RoI extracted from the 4D STEM dataset. Even with the lower pixel density of the 4D STEM image, all of the fibers that can be observed in the SE image can also be observed in the BF image.

Figure 5c shows the ensemble average DP of just the fibers obtained by thresholding the BF image and including only those DPs associated with fibers visible in the thresholded image. Note that this ensemble average DP also contains diffraction information from the amorphous carbon substrate immediately beneath each fiber. The diffuse appearance of the diffraction rings is partially due to the sample (i.e., streaks on different spots will smear or broaden some rings), the convergent electron beam (i.e., the beam convergence semi-angle was approximately 3 milliradians), and Bragg shift associated with the relatively low magnification (i.e., as the primary electron beam is translated from one position to another in the 400 px × 400 px array of raster positions, each DP will be centered at a slightly different location, resulting in broadening of every feature in the average DP). Bragg shift is not usually an issue if DPs from single fibers or small areas are the features of interest in the 4D STEM dataset, but correction is straightforward if desired.

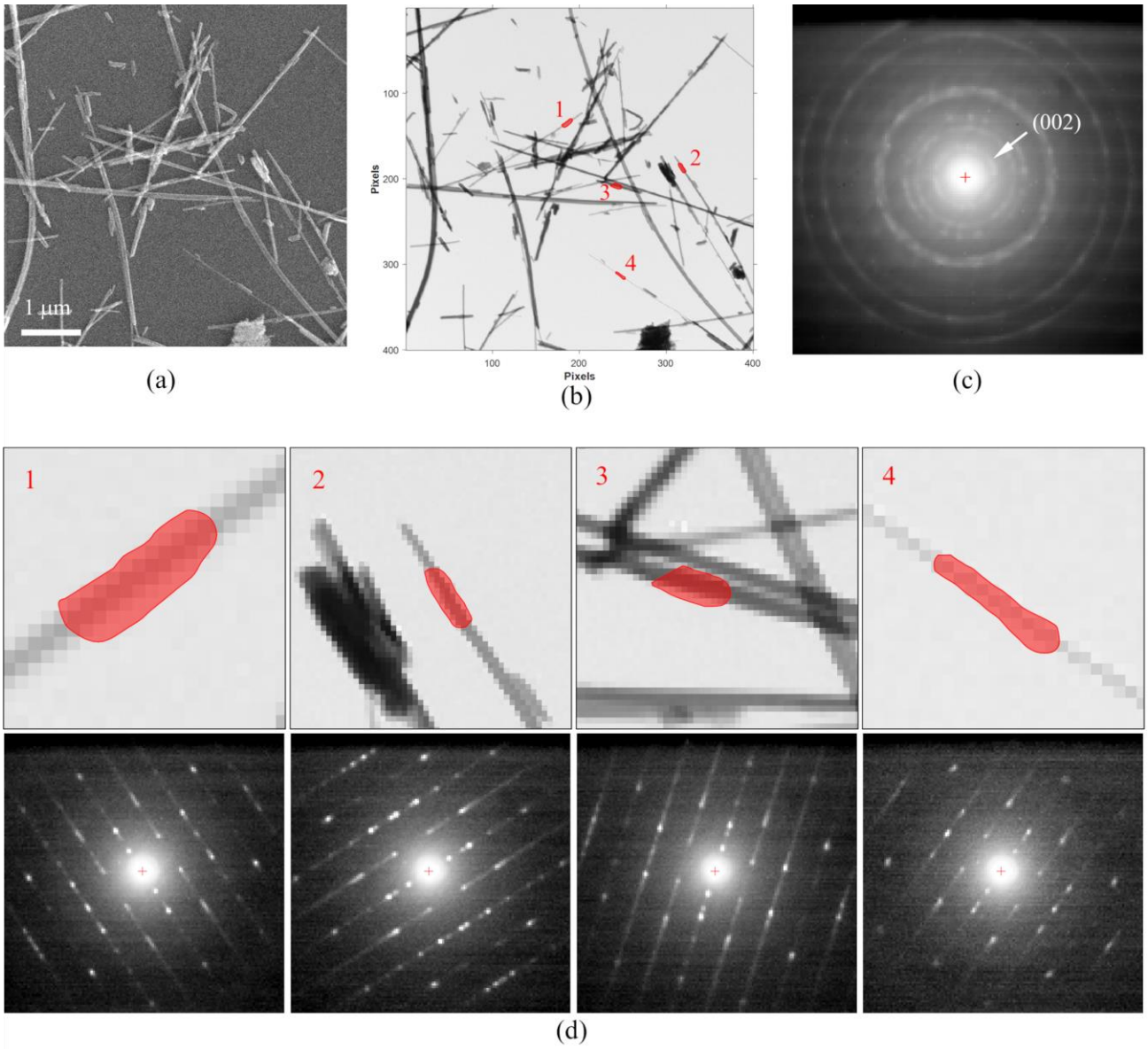

Figure 5. Visualization of chrysotile fibers and DPs using 4D STEM. (a) A low pixel density SE image of fibers on an ultrathin carbon substrate. (b) A marginal bright-field transmission image obtained from the 4D dataset. The inset numbers correspond to the four regions from which single-fiber DPs were obtained. (c) The ensemble average DP of the fibers in (b). The inset arrow points to the (002) diffraction ring. (d) Closer views of different fibers from (b) and their respective DPs. The inset red regions encompass the pixels from which the DPs were obtained.

Figure 5d shows several DPs obtained from different regions indicated in red in Figure 5b. Layer lines and streaking on (110) and (130) reflections are prominent in each DP. Here, small regions of single fibers were manually selected using the marginal BF image, and the average DPs within the different regions were extracted from the 4D dataset. This approach is similar to conventional SAED in the TEM except that here the selected area is chosen offline and can be any arbitrary shape and simultaneously encompass multiple selected areas if desired. As

a side benefit to using an SEM for diffraction, since there are no post-sample lenses in the SEM, the DPs will be correctly aligned with the fiber provided that the SEM scan rotation and diffraction camera are aligned or otherwise taken into account. There is also no ambiguity regarding the specific fiber from which the DP originates when using this approach. This may be useful for automation procedures that can minimize user interaction.

Another way 4D datasets can be used to visualize chrysotile fibers is to select specific DP spots to recreate images that highlight different features of the chrysotile tubular structure. For example, Fig. 6a shows a BF image of chrysotile fibers from a 4D dataset recorded at 30 keV with a 15 μm beam-limiting aperture. The inset shows the average DP of the small region indicated in red on one of the fibers. Specific reflections were chosen from this DP to recreate dark-field (DF) images. For example, the DF image based on the (004) spot shows two bright parallel lines that correspond to the tube walls on opposite sides of the fiber (Fig. 6b). The (110) reflections can be used to obtain diffraction contrast from the "middle" of the same fiber (Fig. 6c). Although not shown here, the (020) spots can also be used to display diffraction contrast along the middle of the fibers. The other images (Fig. 6d and Fig. 6e) show how different reflections can be used to highlight walls on opposite sides of the fiber.

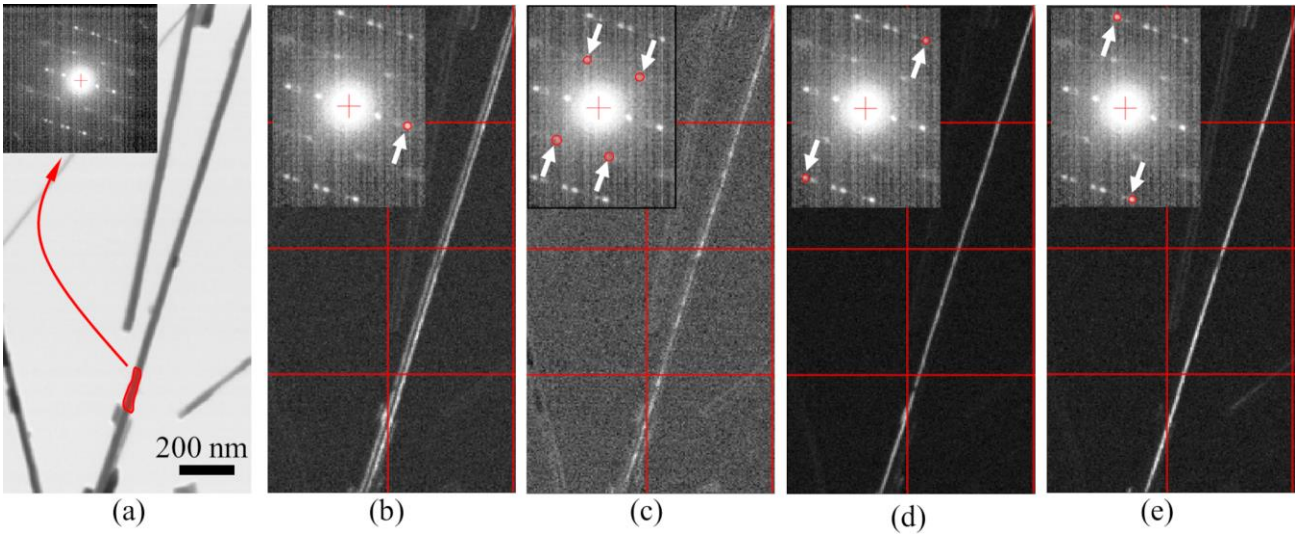

Figure 6. Images and DPs from a 4D STEM dataset showing the use of specific diffraction spots to highlight different parts of chrysotile fibers. (a) A marginal BF STEM image with an inset DP obtained from the region highlighted in red. (b) A DF image using the (004) reflection to highlight walls on both sides of a single fiber. (c) A DF image using (110) reflections to highlight walls in a different orientation. (d) A DF image using the (202) and ($\bar{2}0\bar{2}$) reflections to highlight walls on one side of the fiber. (e) A DF image using the ($20\bar{2}$) and ($\bar{2}02$) reflections to highlight walls on the opposite side of the fiber.

Expanding on the idea using of specific diffraction spots to highlight different parts of chrysotile fibers, a strategically selected annular region applied to the 4D dataset can be used to create an image that highlights the walls of nearly all of the fibers. For example, using the same 4D dataset shown in Figure 5, a narrow annular region encompassing the (002) reflection was

used to create the DF image in Fig. 7. The benefit to using the (002) reflection is that the chrysotile diffraction signal is not overshadowed by contributions from the direct beam or the amorphous carbon substrate. For example, at 30 keV the amorphous carbon substrate exhibits a first local diffraction maximum centered near a scattering angle of 30 milliradians. The (002) scattering angle for chrysotile is approximately 9.5 milliradians at 30 keV, which is both large enough to exclude contributions from the direct beam (the beam convergence semi-angle used here was approximately 3 milliradians) and small enough to exclude most of the scattering from the amorphous carbon substrate. Hence, the walls of nearly every chrysotile fiber exhibit strong contrast with respect to the ultrathin carbon substrate. The capability to selectively highlight asbestos fibers could be used to enhance the visibility of asbestos compared to non-asbestos materials in samples obtained in the field.

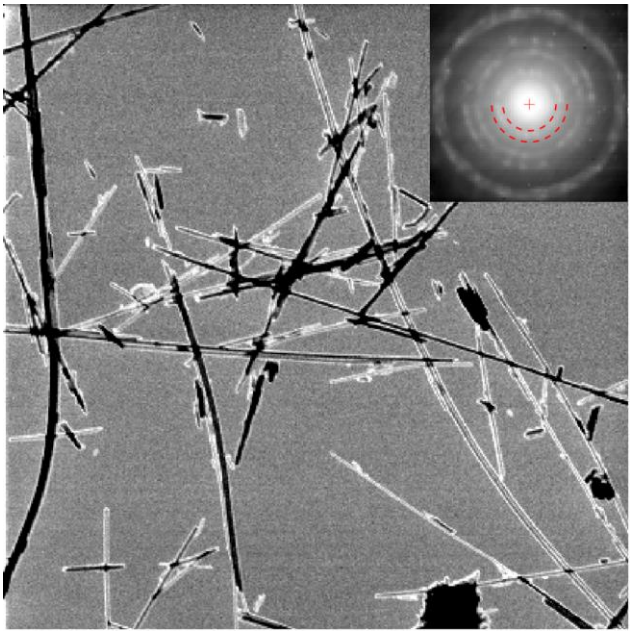

Figure 7. An annular DF image of chrysotile showing strong diffraction contrast from tube walls with respect to the carbon substrate. The image was obtained from the 4D STEM dataset shown in Figure 5 by using an annular aperture encompassing only the (002) diffraction ring shown in the inset DP. The inset red dashed arcs are shown encompassing only half of the annular region used to generate the image so as to keep the (002) reflection visible.

Amosite and Crocidolite

The primary intent in this section is to show that the SEM can also be used to obtain DPs from amphiboles, as demonstrated with amosite and crocidolite. In-depth diffraction pattern interpretation studies have been published elsewhere and will not be pursued here.[13,32-35] The classification protocol for asbestos amphiboles are also more complex than those for chrysotile depending on the required level of analysis. Although amphiboles exhibit the characteristic ~0.53 nm layer line spacing that can be used as a tentative identification parameter, this observation alone is not sufficient to definitively classify fibers as amphiboles.[26,35,36] Definitive classification requires quantitative zone-axis diffraction analysis, or the presence of other known

crystallographic defects that give rise to different diffraction spot distributions along the layer lines. The sample holder used in this work can be used to tilt samples to specific zone axes, but it is time consuming and other configurations may be more convenient.[37]

Amosite results shown in Fig. 8 were obtained at 25 keV (20 μm aperture). Crocidolite results shown in Fig. 9 were obtained at 30 keV (15 um aperture). In both figures, an SE image encompassing a few fibers in different orientations is shown. (Note that although 25 keV and 30 keV beam energies were used here, lower beam energies are actually better suited to examining fiber surface topography). The intention behind using SE images here rather than transmission images was to show that a dedicated semiconductor-style transmission imaging detector like the aSTEM detector used earlier in this contribution is not required for diffraction analysis, further demonstrating the viability of a conventional SEM for fiber asbestos fiber analysis. Any detector capable of producing an image that can be used as a guide to position the primary electron beam can be used. Using those SE images, individual DPs were extracted from videos (2 s frame rate, no binning) recorded as the beam was positioned manually on each of the fibers. A pAl reference DP recorded under identical illumination conditions is superimposed on each of the asbestos DPs. To avoid extensive saturation of the superimposed DPs in the region near the direct beam, the pAl DPs were cropped just inside the pAl (220) reflection before being superimposed on the asbestos DPs. For reference, the inset red cross indicates the center of the pAl DP, and the position of the cropped pAl (111) reflection is indicated with a dashed red arc.

Several features can be observed in the amosite and crocidolite DPs. For example, each DP is aligned correctly with its respective fiber, and the layer line periodicity in each of the DPs corresponds well with the characteristic 0.53 nm spacing between the $d_{(001)}$ planes of the different fibers. The $d_{(001)}$ lattice spacing for each asbestos fiber was calculated based on the layer line separation and the pAl (220) reflection, and are shown inset in the different DPs. Another observation is that the spots within amosite layer lines tend to be more evenly spaced than those in crocidolite layer lines. This is consistent with previous TEM observations and has been suggested as a method by which crocidolite can be distinguished from amosite. However, the crocidolite DPs shown here do not exhibit alternating long and short spot spaces that correspond to periods of 1.66 nm and 2.16 nm, nor do the amosite DPs exhibit equally spaced spots corresponding to a period of 1.80 nm as observed in the TEM.[38] This could be due to differences in the source of asbestos, or differences in defect types and densities at the locations where the DPs were obtained on the different fibers.

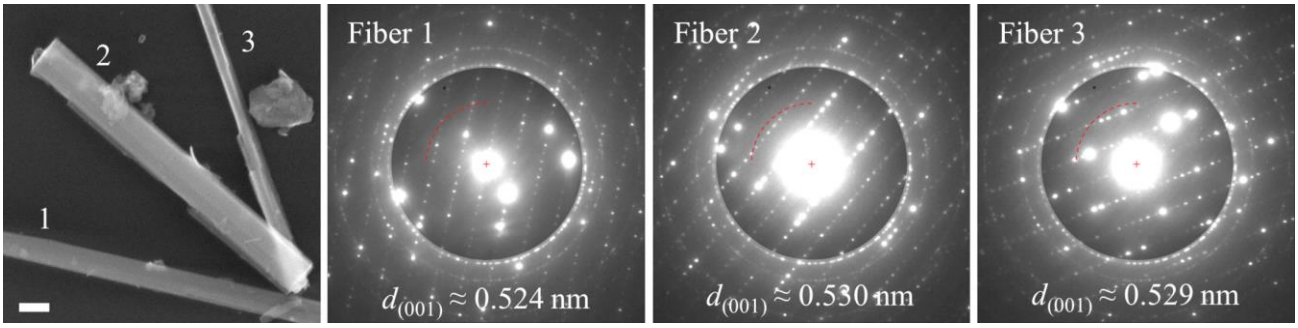

Figure 8. An SE image of amosite fibers and DPs from the numbered fibers recorded at 25 keV with a 20 μm aperture. A polycrystalline aluminum DP cropped just inside the (220) reflection is superimposed on each amosite DP. The inset red arcs indicate the position of the cropped pAl (111) reflection, and the red cross indicates the center of the pAl DP. Scale bar = 200 nm.

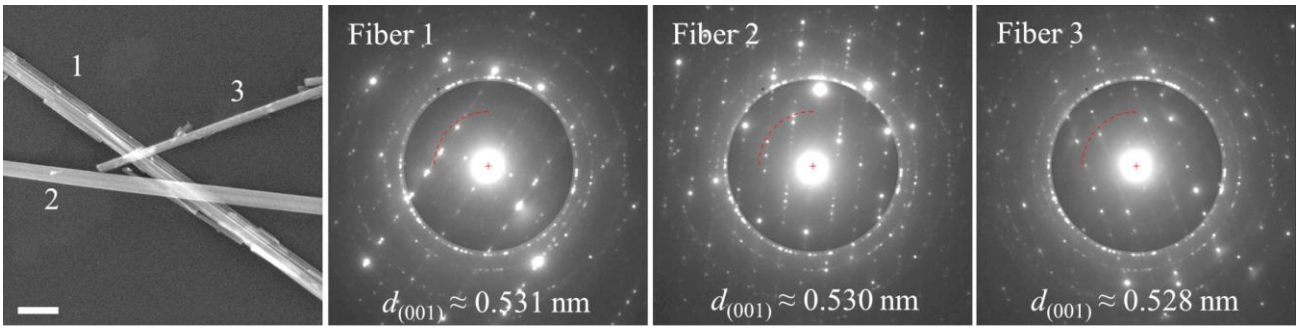

Figure 9. An SE image of crocidolite fibers and DPs from the numbered fibers recorded at 30 keV with a 15 μm aperture. A pAl DP cropped just inside the (220) reflection is superimposed on each crocidolite DP. The inset red arcs indicate the position of the cropped pAl (111) reflection, and the red cross indicates the center of the pAl DP. Scale bar = 200 nm.

Discussion

This work demonstrates that transmission electron images and DPs can be obtained from asbestos fibers in an SEM using different experimental approaches. In particular, the results show that diffraction patterns can be readily obtained from NIST SRM 1866 (chrysotile, amosite and crocidolite) which comprises a set of Standard Reference Materials specifically intended to be used as benchmarks for other studies. Although not shown here, similar results (i.e., layer lines and the accompanying interplanar spacing $d_{(001)} \approx 0.53$ nm) can be obtained from the less common asbestos forms comprising NIST SRM 1867 (anthophyllite, actinolite and tremolite).

Regardless of the EM technique employed to characterize asbestos, there are still challenges associated with sample analyses. For example, fibers do not always exhibit experimentally useful DPs for various reasons. Field samples may be extremely dirty, or fibers may be too thick or in an orientation not conducive to providing interpretable DPs. For this work, the samples are cleaner than what might be encountered in the field, but carbon can still accumulate at spots where the primary electron beam is positioned if the beam is left in one place for too long. For example, the white spots in Fig. 10 are textbook examples of carbon buildup on dirty samples in an SEM. The brightest spots at the left and right sides of the image are due to a

beam dwell time of >5 s, the less bright spots in between were due to a beam dwell time of approximately 2 s. These well-known artifacts can interfere with electron transmission through the sample and compromise the ability to obtain DPs. However, although the beam dwell times used here were intentionally extended beyond what is required to obtain sufficient signal in a 30 kV DP, the DPs obtained from the edges if the fibers still contain enough information for classification purposes. Unless extremely dirty samples or excessive beam dwell times are used, we do not anticipate significantly more difficulty obtaining DPs from field samples with an SEM than with a TEM.

When fibers are too thick, rather than trying to obtain a DP from the thickest part of the fiber it may be feasible to manually position the electron beam on the edge of a fiber to acquire useful diffraction information. For example, Fig. 10 shows two amosite fibers and several DPs obtained from the indicated locations. This figure shows that although the direct electron beam (i.e., the (000) spot) can transmit through the thickest part of the fibers, other reflections may not appear. However, strategic beam placement near the edge of the fibers can provide useful information from fibers that are otherwise largely too thick to transmit an electron beam. When the 4D STEM-in-SEM technique is applied to thick fibers, the electron beam raster array density (i.e., the spacing between points at which DPs are acquired) can be made sufficiently fine to capture meaningful information from the edges of fibers provided that the fiber edges are sufficiently electron transparent.

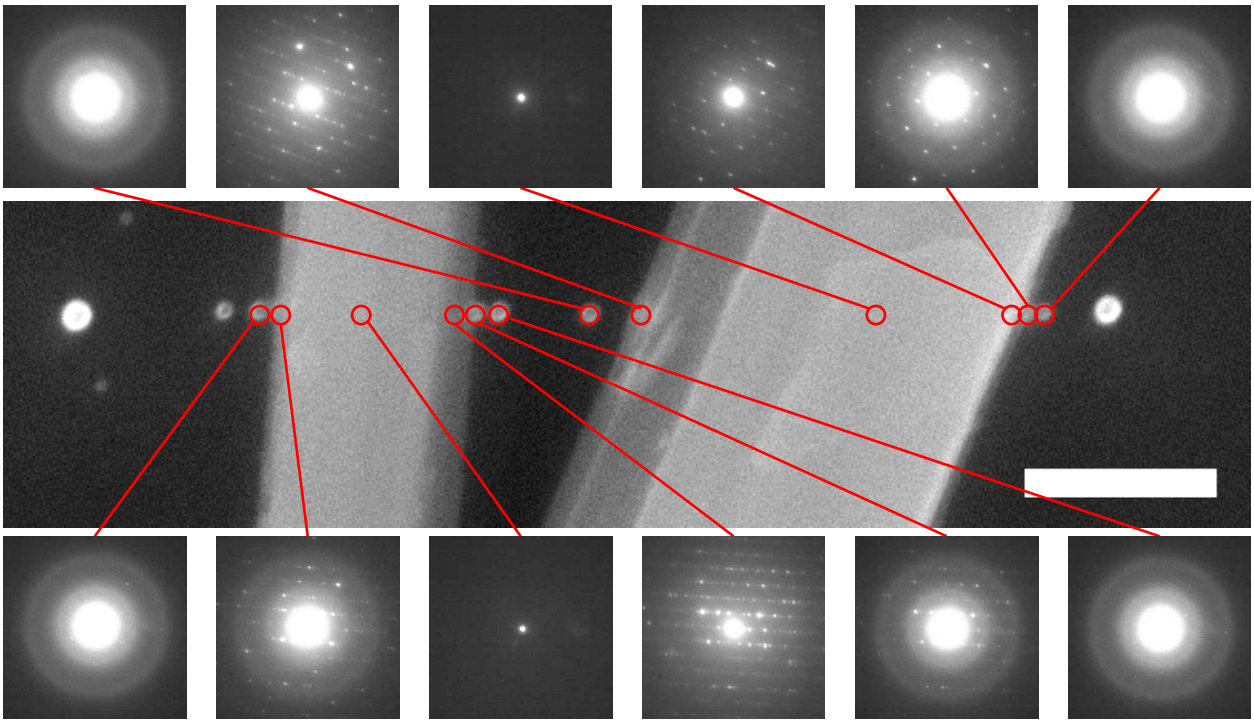

Figure 10. A 30 keV SE image of two amosite fibers on an ultrathin carbon substrate, and DPs from different locations showing how information can still be obtained from fibers that are largely too thick to transmit a 30 keV electron beam. Beam dwell time was approximately 2 seconds at each point. Scale bar = 400 nm.

Regarding the use of diffraction reference samples for accurate lattice measurements of asbestos, an "internal" sputtered Au sample support grid is ideal from the perspective of SEM beam budget time and measurement accuracy, but the added thickness may not be ideal for electron diffraction at the beam energies used an SEM. However, we have shown that an "external" diffraction reference such as pAl can be used to obtain results practically identical to those obtained with sputtered Au. Moreover, although Au sputtering systems are generally easy to use, pAl reference grids are inexpensive, readily available from numerous sources, and require no sample preparation. The only requirement is that a multi-slot sample holder be used to minimize sample exchange challenges.

The detector used to collect DPs for this contribution was made in-house, but other experimental setups can also be used. For example, a detector nearly identical to the one used here has been commercialized by one of the major electron microscopy vendors.[39] Although it is intended for transmission EBSD,[40] it can be configured for 4D STEM by motivated users. Another straightforward approach is to use a small footprint direct electron detector as shown in Figure 11a.[41,42] Here, the detector and sample holder are attached to the SEM sample stage using a dovetail connector, and a USB feedthrough is used to connect the detector to an external workstation where DPs can be recorded using vendor supplied software. A single-slot sample holder is shown in the figure, but other configurations are also feasible. The detector can also be synchronized with the SEM scan coils via python script to obtain 4D datasets, or it can be configured to continuously record DPs in full-frame mode or in event mode as the beam is positioned at different locations on the asbestos sample. For example, Fig. 11b shows a representative chrysotile DP obtained using the continuous full-frame recording configuration of this detector and a 15 keV (20 μm aperture) primary electron beam. Although the 55 μm × 55 μm pixel size of this detector is large compared to the 4.5 μm × 4.5 μm pixel size of the camera used in the rest of this contribution, the characteristic layer lines and spot streaking can still be observed in the DP without a direct beam blocker. A potential benefit to this small detector footprint approach is that portable or desktop SEMs can accommodate these devices. This means mobile asbestos testing stations that enable imaging, EDX, and electron diffraction are entirely feasible and comprehensive characterization can be performed in the field rather than in a dedicated TEM or SEM lab.

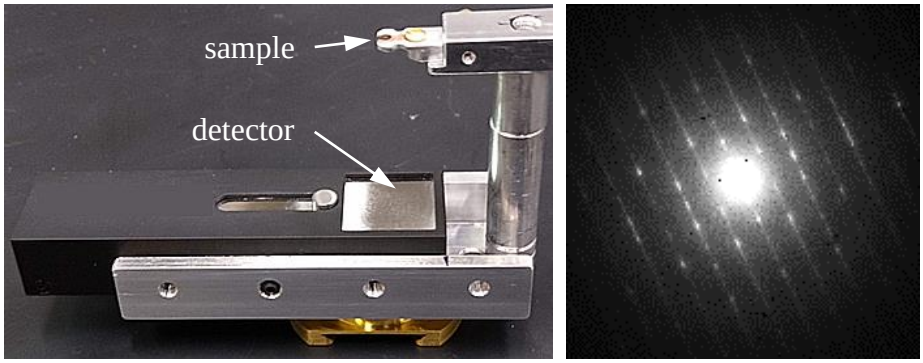

(a) (b)

Figure 11. (a) A small footprint direct electron detector that can be mounted directly to the SEM sample stage. (b) A 15 keV DP obtained from chrysotile using the direct electron detector.

The 4D STEM approach offers a significant benefit beyond the ones strictly demonstrated here. For example, an *entire* TEM grid can be examined rather than a few small regions.[19] With the exception of setting up a small handful of scanning parameters, the data collection process is largely automatic and is a significant throughput improvement over TEM imaging and diffraction techniques specified in the test protocols. Moreover, data analyses can conceivably be automated using image/pattern recognition techniques that enable asbestos fibers to be differentiated from non-asbestos fibers. Once the asbestos fibers are identified and their coordinates located on the sample support grid, it should also be feasible to automatically collect EDX spectra and fiber size distributions.[16] Looking forward, and with appropriate training data, machine learning and artificial intelligence approaches can conceivably be used to fully automate the entire electron microscopy analysis procedure for asbestos. To that end, each of the 4D data sets acquired here could be used as training data.

Lastly, although 3 mm diameter TEM grids are extremely useful for supporting samples in the electron beam, they are not an absolute requirement in an SEM. As long as an electron transparent sample can be prepared, the shape can be arbitrary provided it can be supported between the SEM pole piece and the detector. To that end, the sample can conceptually be placed directly on the scintillator as demonstrated in yet another recently reported STEM-in-SEM development.[43] Tilting samples to obtain specific zone axis diffraction patterns may be challenging with this approach, but it could be ideal for chrysotile and perhaps amphiboles in some circumstances.

Conclusions

We have shown that SEMs can be used for transmission electron diffraction studies of asbestos. Interpretable DPs obtained at ≤ 30 keV beam energies were obtained from chrysotile, amosite, and crocidolite fibers in a modern SEM without difficulty. Even fibers that were largely too thick to obtain a meaningful DP at the thickest part of the fiber could still be analyzed by strategic placement of the electron beam at the edge of the fiber. We have also shown that different electron detection schemes can be successfully used to obtain DPs, and that emerging electron microscopy trends such as 4D STEM-in-SEM can be applied to asbestos identification

and classification studies. The STEM-in-SEM characterization methods described here could provide a path towards more efficient and cost-effective airborne asbestos monitoring in terms of lower equipment cost, less stringent operator training requirements, increased sample throughput, and greater field of view compared to TEM. Further work could also lead to improvements in automation, fiber identification and size distribution quantification. Moreover, this approach can be used in the field for immediate analysis with portable SEMs.

References

**Identification of certain commercial equipment, instruments, or materials does not imply recommendation or endorsement by NIST, nor does it imply that the identified materials or equipment are necessarily the best available for the purpose.

(1) E. J. W. Whittaker, Structure and Properties of Asbestos, Reprinted from Fibre Structure, J.W.S. Hearle and R.H. Peters (eds), 'Asbestos'. Copyright Butterworth & Co. (Elsevier) and the Textile Institute, **1963,** pp. 594–620. https://doi.org/10.1533/9781845697310.3.425

(2) D. R. Van Orden, Asbestos. Chapter 2 in Environmental Forensics. Eds. Morrison, R.D. and Murphy, B. L. Academic Press, **2005**. ISBN 978-0-12-507751-4. https://doi.org/10.1016/B978-012507751-4/50024-0

(3) Clean Air Act, L. 91–604, §1, Dec. 31, 1970, 84 Stat. 1676. https://www.govinfo.gov/content/pkg/STATUTE-84/pdf/STATUTE-84-Pg1676.pdf

(4) National Emission Standards for Hazardous Air Pollutants (NESHAP) for asbestos, 38 FR 8826, April 6, 1973.

(5) K. Quarmby, Asbestos in drinking water: What does it mean for human health? Accessed online 25 Jan, 2024. https://bbc.com/future/article/20240124-asbestos-in-drinking-water-an-overlooked-health-risk

(6) Environmental Protection Agency. Guidelines for Conducting the AHERA TEM Clearance Test to Determine Completion of an Asbestos Abatement Project. EPA 560/5-89-001. **1989**. https://nepis.epa.gov/Exe/ZyPURL.cgi?Dockey=91013C0D.TXT

(7) J. R. Millette, Asbestos analysis methods. Chapter 2, in *Risk Assessment, Epidemiology, and Health Effects*. CRC Press (Boca Raton, Fl.), **2012**, pp. 23-48. https://doi.org/10.1201/b10958

(8) International Organization for Standardization. Ambient air determination of asbestos fibers. Indirect-transfer transmission electron microscopy method. ISO 13794:2019.

(9) National Institute for Occupational Safety & Health. NIOSH 7402, Asbestos by TEM, 1994.

(10) Environmental Protection Agency. Code of Federal Regulations: Chapter 40, Part 763. https://www.epa.gov/sites/default/files/documents/2003pt763_0.pdf

(11) American Society for Testing and Materials, "Standard Test Method for Airborne Asbestos Concentration in Ambient and Indoor Atmospheres as Determined by Transmission Electron Microscopy Direct Transfer (TEM)" D6281-23. https://www.astm.org/d6281-15.html

(12) P. N. Breysse, Electron microscopic analysis of airborne asbestos fibers. *Critical Reviews in Analytical Chem.* **1991,** *22* (3,4) 201–227. https://doi.org/10.1080/10408349108055029

(13) C.O. Ruud, C. S. Barrett, P. A. Russell, R. L. Clark, Selected Area electron diffraction and energy dispersive X-ray analysis for the identification of asbestos fibers, a comparison. *Micron* **1976**, *7*, 115-132. https://doi.org/10.1016/0047-7206(76)90055-8

(14) C. O. Ruud, An Overview of Electron Microscopy Methods, NBS Special publication 506, Proceeding of Workshop on Asbestos: Definitions and Measurement Methods, **1978**, pp. 221-234. https://nvlpubs.nist.gov/nistpubs/Legacy/SP/nbsspecialpublication506.pdf

(15) P. A. Baron, Measurement of Airborne Fibers: A Review. *Ind. Health* **2001**, *39*, 39–50. https://doi.org/10.2486/indhealth.39.39

(16) R. Cossio, C. Albonico, A. Zanella, S. Fraterrigo-Garofalo, C. Avataneo, R. Compagnoni, F. Turci, Innovative unattended SEM-EDS analysis for asbestos fiber quantification, *Talanta* **2018**, *190*, 158-166. https://doi.org/10.1016/j.talanta.2018.07.083

(17) J. D. Holm and B. W. Caplins, STEM-in-SEM: Introduction to Scanning Transmission Electron Microscopy for Microelectronics Failure Analysis. **2020** ASM International, Materials Park, OH. ISBN-13: 978-1-62708-292-1 (pdf). https://doi.org/10.31399/asm.tb.stemsem.9781627082921

(18) B.W. Caplins, J.D. Holm and R.R. Keller, *Microscopy and Microanalysis*, **2018,** 24(S1), 658–659. https://doi.org/10.1017/S1431927618003781.

(19) B.W. Caplins, J.D. Holm, R.M. White and R.R. Keller, *Ultramicroscopy* **2020**, *219*, 113137. https://doi.org/10.1016/j.ultramic.2020.113137

(20) C. Ophus, *Microscopy and Microanalysis* **2019**, *25*, 563–582. doi:10.1017/S1431927619000497

(21) G.W. Bailey, R.V.W. Dimlich, K.B. Alexander, J.J. McCarthy, T.T. Pretlow, M. Raanes and J. Hjelen, *Microscopy and Microanalysis* **1997**, *3*(S2) 767–768. https://doi.org/10.1017/S1431927600010722

(22) B. R. Bandli and M.E. Gunter, M E., *Microscopy and Microanalysis* **2014**, *20*(6) 1805-1816. https:/doi.org/10.1017/S1431927614013415

(23) E.B. Steel and J.A Small, *Anal. Chem.* **1985**, *57*, 209-213. https://doi.org/10.1021/ac00279a049

(24) K. Yada, *Acta. Cryst.* **1967**, *23*, 704. https://doi.org/10.1107/S0365110X67003524

(25) R. L. Clark, MSHA standard method for fiber identification by electron microscopy. NBS special publication 619. Proc of the NBS/EPA Asbestos Standards Workshop 1980. Issued March 1982. pp. 207-210. https://nvlpubs.nist.gov/nistpubs/Legacy/SP/nbsspecialpublication619.pdf

(26) S. Ring and R.J. Suchanek, Fiber identification and blank contamination problems in the EPA provisional method for asbestos analysis. NBS Publication 619. Proc. of the NBS/EPA asbestos standards workshop, 1980. Issued 1982. pp. 190-206. https://nvlpubs.nist.gov/nistpubs/Legacy/SP/nbsspecialpublication619.pdf

(27) J. Martin, M. Beauparlant, S. Sauvé, G. L'Espérance,. *Micron* **2017,** *94*, 26-36. https://doi.org/10.1016/j.micron.2016.11.011

(28) J. Martin, M. Beauparlant, S. Sauvé, G. L'Espérance,. *Micron* **2017,** *96*, 1-8. https://doi.org/10.1016/j.micron.2017.01.006

(29) J. Holm. *Microscopy and Microanalysis* **2023**, *29* 131-137. https://doi.org/10.1093/micmic/ozac010

(30) D. B. Williams and C. B. Carter, Transmission Electron Microscopy: A Textbook for Materials Science. Plenum Press, New York. **1996**, pg 150. ISBN 0-306-45247-X

(31) E. J. Chatfield, Analytical procedures and standardization for asbestos fiber counting in air, water, and solid samples. NBS special publication 619. Proc of the NBS/EPA Asbestos Standards Workshop 1980. Issued March 1982. pp. 91-107. https://nvlpubs.nist.gov/nistpubs/Legacy/SP/nbsspecialpublication619.pdf

(32) R.L. Clark and C. O. Ruud, *Micron* **1974**, *5*, 83-88. https://doi.org/10.1016/0047-7206(74)90036-3

(33) J. L. Hutchison, M. C. Irusteta and E. J. W.Whittaker, *Acta Cryst.* **1975**, *A 31*, 794-801. https://doi.org/10.1107/S0567739475001714

(34) J. L. Hutchison and E. J. W. Whittaker, *Environmental Research* **1979**, *20*, 445-449. https://doi.org/10.1016/0013-9351(79)90018-5

(35) J. E. Chisholm, *J. Mat. Sci.* **1973**, *8*, 475-483. https://doi.org/10.1007/BF00550451

(36) A. M. Langer, A. D. Mackler, and F. D. Pooley, *Environmental Health Perspectives*, **1974**, *9*, 63-80. https://doi.org/10.1289/ehp.7496

(37) J. Müller, B. Haas, W. Van den Broek, S. Shabih and C.T.Koch, *Microscopy and Microanalysis* **2020**, *26*(S2), 1906-1907. doi:10.1017/S1431927620019789

(38) M. I. Skikne, J. H. Talbot and R. E. G. Rendall, *Eviron. Res.* **1971**, *4*, 141-145. https://doi.org/10.1016/0013-9351(71)90042-9

(39) J.J. Fundenberger, E. Bouzy, D. Goran, J. Guyon, H. Yuan and A. Morawiec, *Ultramicroscopy* **2016**, *161*, 17–22. https://doi.org/10.1016/j.ultramic.2015.11.002

(40) R. R. Keller and R.H. Geiss. *Journal of Microscopy*, **2012,** *245*(3), 245–251. https://doi.org/10.1111/j.1365-2818.2011.03566.x

(41) MiniPix TPX3, https://hawkeyesi.com/minipix-tpx3/ Accessed 18 Mar. 2024.

(42) A. Orekhov, D. Jannis, N. Gauquelin, G. Guzzinati, A. Nalin Mehta, S. Psilodimitrakopoulos, L. Mouchliadis, P.K. Sahoo, I. Paradisanos, A.C. Ferrari, G. Kioseoglou, E. Stratakis and J. Verbeeck, *arXiv* **2020** https://doi.org/10.48550/arXiv.2011.01875

(43) A. J. Kievits, B.H. Duinkerken, J. Fermie, R. Lane, B.N.G. Giepmans and J.P. Hoogenboom, *Ultramicroscopy* **2024**, *256*, 113877. https://doi.org/10.1016/j.ultramic.2023.113877